Unraveling the distinct roles of Mg occupation on Li or Co sites on high-voltage $LiCoO_2$

Weijin Kong [a], Dong Zhou[b], De Ning[b,c], Wenyun Yang[d], Deniz, Wong[b], Jicheng Zhang [a], Qingyuan Li[a], Jinbo Yang[d] , Christian Schulz[b], and Xiangfeng Liu[a,e]*

[a] Center of Materials Science and Optoelectronics Engineering, College of Materials Science and Optoelectronic Technology, University of Chinese Academy of Sciences, Beijing 100049, P. R. China

[b] Helmholtz-Center Berlin for Materials and Energy, Hahn-Meitner-Platz 1, Berlin 14109, Germany

[c]Center for Photonics Information and Energy Materials, Shenzhen Institutes of Advanced Technology, Chinese Academy of Sciences, Shenzhen 518055, P.R. China

[d] State Key Laboratory for Mesoscopic Physics, School of Physics, Peking University, Beijing 100871, China

[e]CAS Center for Excellence in Topological Quantum Computation, University of Chinese Academy of Sciences, Beijing 100190, China

*Corresponding Author: liuxf@ucas.ac.cn. (X.L.) Tel. +86 10 8825 6840

Abstract

A high-voltage $LiCoO_2$ cathode material has been increasingly studied due to its high capacity; however, the structural instability of this material results in poor cycling performance at high voltages, restricting its application. We use a controlled Mg doping strategy to modulate the crystal and electronic structure of the material and unravel the different effects of Mg occupation at Li and Co sites on the structure and electrochemical performance of $LiCoO_2$. Mg substitution at Li sites provides much better electrochemical performance than Mg substitution at Co sites. Compared with bare $LiCoO_2$, the substitution of Mg for Li and Co significantly enhances the capacity retention from 0.5% to 58.6% and 85.6% (500 cycles at 5C), respectively. Mg substitution at Li sites provides a "pillar" to stabilize the layered structure and increases the interlayer spacing ($I_{(LiO2)}$) to reduce the energy barrier for Li^+ migration. The stress and strain on the crystal structure caused by the substantial expansion and contraction during cycling are alleviated, while the stability of oxygen in the $Li_{0.96}Mg_{0.04}CoO_2$ sample is enhanced; additionally, the destruction of the CoO_6 octahedron is also significantly inhibited, all of which confirm the increase in stabilization due to the Mg substitution in $LiCoO_2$. This study offers some insights on the distinct effects of the same dopant at different crystal sites, which is instructive to develop a precisely controlled doping strategy.

Key words: high voltage; $LiCoO_2$; Mg doping; "pillar" effect; cycling stability

TOC

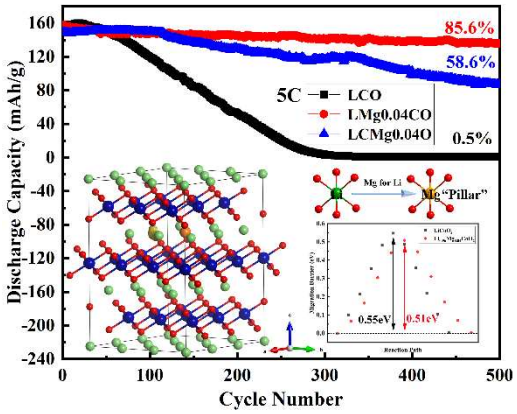
85.6%
58.6%
5C
LCO
LMg0.04CO
LCMg0.04O
0.5%
Discharge Capacity (mAh/g)
Cycle Number
Mg for Li
Mg "Pillar"
0.55eV
0.51eV

1.Introdution

Cathode materials with high energy density are a common and continuous focus for rechargeable batteries, especially lithium-ion batteries, due to the rapid increase in the requirements of portable electronic equipment, electric vehicles and large-grid energy storage.(1-4). Among numerous cathode materials ($LiCoO_2$(5, 6), $LiMnO_2$(7, 8), $LiMn_2O_4$(9-12), $LiFePO_4$, Li-rich(13), Ni-rich(14-18) and so on) for lithium-ion batteries, $LiCoO_2$ cathode materials with simple elemental compositions and high energy densities have been increasingly studied.(19-21).

It is recognized that increasing the charging cutoff voltage of $LiCoO_2$ cathode materials is an effective way to improve the specific capacity for lithium-ion batteries(22-24). However, with an increasing charging cutoff voltage, the structure of $LiCoO_2$ will become increasingly unstable and distorted because more lithium ions are extracted from the host structure(25-27). The fundamental reason behind this limitation of a high charging cutoff voltage is that when more than half of the lithium ions are extracted from the original layered crystal, an irreversible phase transition will occur, destroying the CoO_6 octahedron and generating stress and strain in the crystal structure. Furthermore, the destruction of the layered structure will result in a rapid decrease in the long-term cycling capacity retention ratio. To enhance the reversibility of structural evolution and improve the stability of the CoO_6 octahedron at high voltage, considerable effort has been expended to investigate the application of surface coatings, doping of inactive elements in the host structure, and use of suitable electrolyte additives.(28-30).

Many attempts have been made to stabilize the structure and suppress the phase transition of high-voltage $LiCoO_2$ in the past few decades; these efforts include doping inactive transition metal elements (Al(31), Zr(32), Ti(33), Sr(34), La(35), etc) to enhance structural stability and applying metallic oxide coatings (ZrO_2, TiO_2(36), Al_2O_3(37), MgO(38), etc) or lithium compounds ($LiAlO_2$, Li_2ZrO_3(39), Li_3VO_4(40), etc) to reduce the occurrence of side reactions between the cathode material and electrolyte solution. Among all the modification approaches, doping transition metal elements is the most common and has been proven to be effective for improving the electrochemical performance of $LiCoO_2$(41-43). Li et al. reported that the cycling of $LiCoO_2$ at a high cutoff voltage (versus Li/Li^+) was stable by co-doping trace Ti-Mg-Al(26). Lu et al. also reported the enhanced electrochemical performance of $LiCoO_2$ cells at a high cutoff voltage through a ternary Li-, Al-, and F-based hybrid treatment(30). A bifunctional self-stabilization strategy involving codoping Al+Ti in the bulk material and doping a gradient of Mg on the surface of the material has been proposed to enhance the performance of high-voltage $LiCoO_2$(27). Recently, Huang et al. improved the cycling stability of high-voltage $LiCoO_2$ by doping Mg at Li sites.(44). The atom occupation of the dopant at the different crystal sites also has a distinct effect on the structure and electrochemical performances, along with the types or valence of the doped atoms having an effect. However, the roles of the dopant at different sites are still poorly understood.

Herein, the different effects of Mg substitution at Li and Co sites in high-voltage $LiCoO_2$ are systematically investigated, and the roles of Mg are revealed by means of

neutron powder diffraction (NPD), resonant inelastic X-ray scattering (RIXS), *in situ* and *ex situ* X-ray diffraction (XRD), and density functional theory (DFT) calculations. Mg substitution at Li sites has a much better effect on both the stability of the lattice oxygen in the host structure and the migration ability of lithium ions, which enables a largely enhanced cycling stability at a high charge-discharge rate.

2. Results and Discussion

2.1 Crystal Structure and Morphology

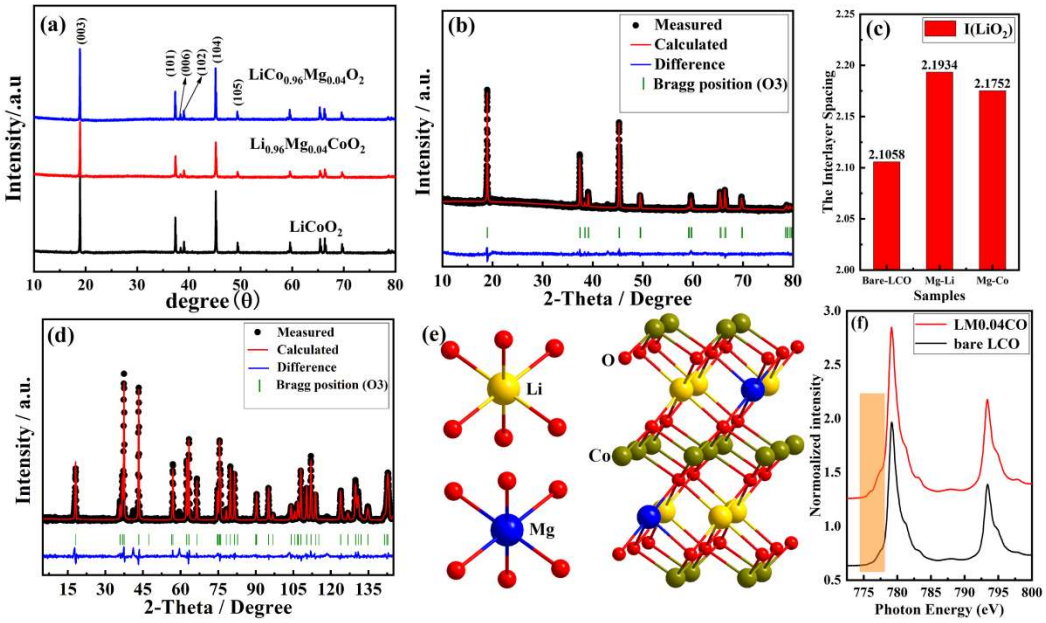

Figure 1. (a) The XRD patterns; (b) The refinement results of XRD for LM0.04CO; (c) The comparison of the interlayer spacing of the three sample; (d) The refinement results of the neutron powder diffraction (NPD) for LM0.04CO; (e) The Refined crystal structure of LM0.04CO by NPD; (f) Co-$L_{3,2}$ SXAS spectra of bare LCO and LM0.04CO.

To investigate the crystal structures of bare $LiCoO_2$ (LCO), $Li_{0.96}Mg_{0.04}CoO_2$ (LM0.04CO) and $LiCo_{0.96}Mg_{0.04}O_2$ (LCM0.04O) cathode materials, we collected X-ray diffraction (XRD) patterns. As shown in Figure 1 (a), the peaks of all samples are consistent with the layered α-$NaFeO_2$ structure

that has the R$\bar{3}$m space group without any impurity peaks(23, 45). As shown in Figure S1(a) and (b) and Figure 1(b), Rietveld refinements were performed by Follprof software to reveal the structural parameters of the three samples(46). The fitting factor R_p is 2.28, 3.11, and 1.38%, and R_{wp} is 1.81, 1.72 and 2.47%, which means the refined data can be referenced and acceptable. The spacing of the interlayer ($I_{(LiO2)}$) has a large effect on the migration ability of lithium ions, and the increase in $I_{(LiO2)}$ can provide a wider channel for Li^+ intercalation/extraction during the charge/discharge process, which will lower the energy barrier and reduce the resistance of Li^+ diffusion(47). Compared with LCO (2.1058 **Å**), the interlayer spacings of LM0.04CO (2.1934 **Å**) and LCM0.04O (2.1752 **Å**) all increase, especially the $I_{(LiO2)}$ of the LM0.04CO sample, which has a more obvious increase, as shown in Figure 1(c), indicating that the influence of Mg at the Li site on the interlayer spacing is greater than that of Mg at the Co site.

Table 1 The refined crystallographic parameters of the cathode materials by the XRD patterns.

Samples	LCO	LM0.04CO	LCM0.04O
a/Å	2.8116 (1)	2.8149(1)	2.8182 (1)
c/Å	14.0289(6)	14.0560(7)	14.0639 (6)
O_{ZOX} [a]/ Å	0.24172	0.24469	0.244
$S_{(MO2)}$ [b] / Å	2.5705	2.4919	2.5128
$I_{(LiO2)}$ [c]/ Å	2.1058	2.1934	2.1752
V(Å^3)	96.04(0)	96.45(1)	96.73(1)
Density(g/cm^3)	5.117	5.514	5.148
Rp (%)	2.28	1.38	1.72

Rwp(%)	3.11	1.81	2.47

[a] O_{ZOX} stands for the oxygen position.

[b] $S_{(MO2)}$ stands for the slab thickness: =2[(1/3) - O_{ZOX}]*c*

[c] $I_{(LiO2)}$ stands for the interslab space thickness: = (*c*/3 - $S_{(MO2)}$)

Compared with the LCO cathode material, the crystallographic parameter values of *a* and *c* in LM0.04CO and LCM0.04O increase, as shown in Table 1, which indicates that Mg^{2+} is doped in the host structure. The occupation information of each atom in the crystal structure of all samples is shown in Tables S1-S3. The size of the interlayer spacing ($I_{(LiO2)}$) increases due to the increase in the c value and the change in O_{zox}, which benefits the migration of lithium ions(48). This result is also consistent with the decrease in the lithium-ion migration barrier energy obtained by the first-principles calculation (DFT). Therefore, the rate performance of the assembled half-batteries will be greatly improved. The thickness of the $S_{(MO2)}$ is reduced by the substitution of Mg for Li and Co, which is conducive to the stability of the layered structure in cathode materials(49). The $S_{(MO2)}$ of LM0.04CO (2.4919 Å) is much smaller than that of LCM0.04O (2.5128 Å), indicating better stability. This result also indicates the distinct effect of substituting Mg for Li and Co on the lattice structure of LCO. The shrinkage of $S_{(MO2)}$ is beneficial to the cycling stability of the layered cathode material. Compared with LCO, the calculation density of the other two cathode materials also increases, especially LM0.04CO, which reflects the superior lithium storage capacity in a unit volume of this cathode material.

Table 2 Atoms occupancy of LCO from Rietveld refinement by the NPD

Atom	Site	*x*	*y*	*z*	Occ
Li	3a	0	0	0	1

Co	3b	0	0	0.5	1
O	6c	0	0	0.23944	1

Table 3 Atoms occupancy of LM0.04CO from Rietveld refinement by the NPD

Atom	Site	*x*	*y*	*z*	Occ
Li	3a	0	0	0	0.97114
Mg	3a	0	0	0	0.02886
Co	3b	0	0	0.5	1
O	6c	0	0	0.23955	1

To confirm the substitution of Mg for Li, neutron powder diffraction (NPD) was performed at a wavelength of 1.479728 Å, a range of 8°-145°, and a step width of 0.05°; NPD with these parameters is sensitive to light elements, as shown Figure S1(c). The Rietveld refinement results are shown in Figure S1(d) and Figure 1(d), and the atomic occupancies of the LCO and LM0.04CO samples are shown in Tables 2 and 3. In Table 3, the occupancy of Mg at the Li site of the LM0.04CO cathode material is 0.02886, which proves that Mg is successfully doped at the Li site due to the similar ionic radius(0.76Å for Li-ion; 0.72Å for Mg-ion)(50-52); the refined crystal structures are shown in Figure 1(e). The substitution of Mg for Li can provide a “pillar” to stabilize the crystal structure of the material and provide a “channel” for fast lithium-ion intercalation/extraction during the charge/discharge process. The obtained crystal parameters and refinement results by NPD also show a similar trend to that in the XRD data. Figure 1(f) shows the Co-$L_{3,2}$ soft XAS spectra of the bare LCO and LM0.04CO samples. The main peaks of both samples are located at the same energy, but the difference between bare LCO and LM0.04CO clearly appears as a pre-edge peak at 778.5 eV for the latter, which is a characteristic feature of Co^{2+} with an octahedral local

coordination in the LM0.04CO cathode material; this observation indicates that the substitution of Mg for Li satisfies the charge balance requirement(44).

To reveal the different effects of Mg^{2+} doping at Li or Co sites on the electrochemical performance, the rate capability and cycling performance of the bare LCO, LM0.04CO and LCM0.04O electrode materials were tested. As shown in Figure 2(a), compared with the bare LCO cathode materials, the rate capability of the LM0.04CO and LCM0.04O cathode materials significantly improves at various current rates from 0.1-10C (1C=200 mA g^{-1}) for 5 cycles at each current rate; this improvement is especially observed at a high current density. The discharge specific capacity increases from 14.5 mAh/g to 127.3 mAh/g at 10C, which also strongly verifies the ability of the electrode material to rapidly charge and discharge. Clearly, the discharge capacity of the bare LCO electrode material decreases significantly with an increasing circulating current due to the low diffusion ratio of lithium ions, but the capacity of the LM0.04CO and LCM0.04O electrodes decreases slowly. The increase in the interlayer spacing ($I_{(LiO2)}$: 2.1058 Å for bare LCO, 2.1934 Å and 2.1752 **Å** for LM0.04CO and LCM0.04O) and the decrease in the migration energy barrier of Li^{+} create a structural environment for the rapid charge/discharge process to exhibit excellent rate capacity. As shown in Figure 2(b) and (c), the capacity-voltage curve of the LM0.04CO electrode material is smoother than that of the bare LCO electrode material, and the polarization phenomenon also decreases, which is consistent with the CV curves.

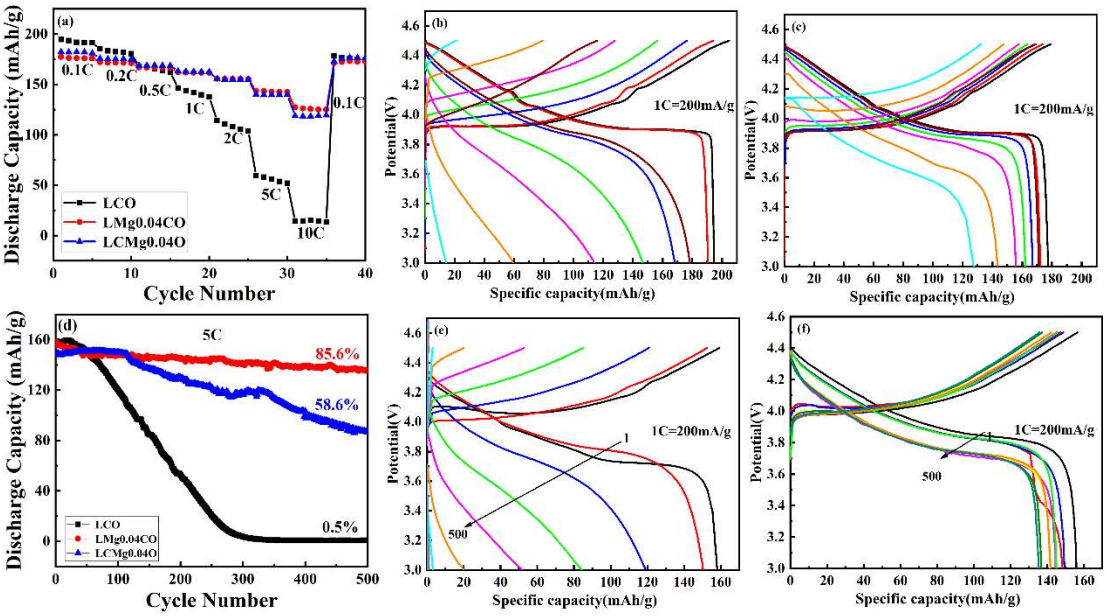

Figure 2 (a) Rate capabilities test at different current densities (Bare LCO， LM0.04CO; 1C = 200 mA g^{-1}), Charge and discharge curves at different rate: (b) Bare LCO;(c) LM0.04CO; (d) cycling performance at 5C, (e) cycling charge and discharge profiles of Bare LCO, (f) cycling charge and discharge profiles of LM0.04CO

Subsequently, the galvanostatic cycling performances of LCO, LM0.04CO and LCM0.04O at 1C and 5C were tested, as shown in Figure S2, and Figure 2(d). At 1C, the capacity retention of LCO and LM0.04CO after 100 cycles is 52.4% and 83.1%, respectively. As shown in Figure 2(d), compared with the bare LCO cathode material, the capacity retention of the LM0.04CO cathode material significantly increases from 0.5% to 85.6% after 500 cycles at 5C. However, the capacity retention of the LCM0.04O cathode at 5C only increases to 58.6%. The large charge/discharge capacity means that lithium ions can be rapidly intercalated/extracted in the layered structure without damaging the stability of the structure at a high current density. The improvement in the capacity retention is largely attributed to the increase in the interlayer spacing and the decrease of $S_{(MO2)}$ induced by the substation of Mg for Li,

which improves the structural stability and cycling performance at a high current density.

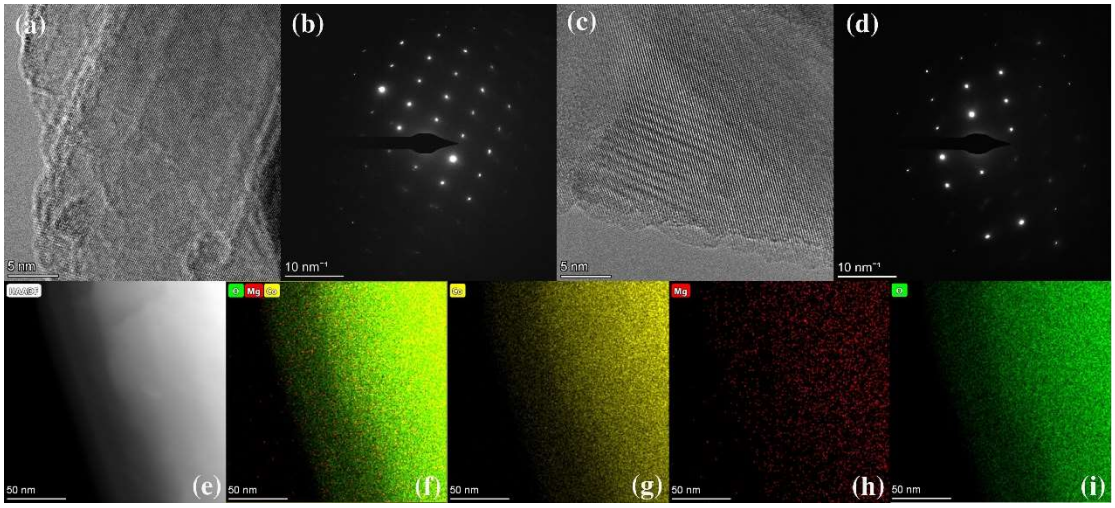

Figure 3 (a) HRTEM images of the Bare LCO sample, (b) selected-area electron diffraction (SAED) pattern of the LCO sample and (c) HRTEM images of the LM0.04CO sample, (d) selected-area electron diffraction (SAED) pattern of the LM0.04CO sample; (e)-(i) HAADF image and the EDS mapping of the Co, Mg, O

To detect the morphology of the bare LCO and LM0.04CO samples, scanning electron microscopy (SEM) was performed, as shown in Figure S3(a) and (b), respectively. Compared with the bare LCO sample, the particle size of the LM0.04CO material is greatly reduced, which is consistent with the increase in the calculation density by XRD. A high-resolution TEM (HRTEM) image and the selected-area electron diffraction (SAED) patterns of the LCO and LM0.04CO samples are shown in Figure 3(a), (c) and (b), (d), respectively. Compared with the bare LCO sample, there are no essential changes in the micromorphology and selected electron diffraction spots of the LM0.04CO cathode material. To directly observe the distribution of each element in the LM0.04CO cathode materials directly, EDS mapping spectra were obtained for verification, and the results are shown in Figure 3(e)-(f). The distributions of Co, Mg,

and O are shown separately in Figure 3 (g)-(i), respectively. Mg is uniformly distributed in the cathode materials, which clearly illustrates the doping of Mg^{2+} in the host structure.

X-ray photoelectron spectroscopy (XPS) analysis was performed to determine the surface chemical states of the LCO and LM0.04CO samples. Figure S4 (a) shows the XPS spectra of the collected Co2p electron orbital for the two samples. The Co2p3/2 and Co2p1/2 peaks are the main peaks located at approximately 780 eV and 795 eV, respectively(23, 53). Surface oxygen and lattice oxygen exist in the cathode materials, as shown in Figure S4(b), and their contents are summarized in Table S4. As shown in Table S4, compared with the bare LCO cathode material, the relative ratio of lattice oxygen is significantly improved from 47.7% to 59.6% in the LM0.04CO cathode material, which indicates that the bonding energy between the alkali metal and oxygen is significantly enhanced(41, 54). Mg^{2+} in the LM0.04CO cathode material can play an important role in stabilizing oxygen in the host structure, which further enhances the stability of the layered structure and improves the cycling stability of the electrode material. The main Mg 1s peak is located at approximately 1302 eV, as shown in Figure S5, which illustrates the existence of Mg^{2+} in the LM0.04CO cathode material(55). Although XPS reveals the state of the elements on the surface of materials, it can also reflect the information inside materials to some certain extent.

2.2 Electrochemical performances and mechanisms

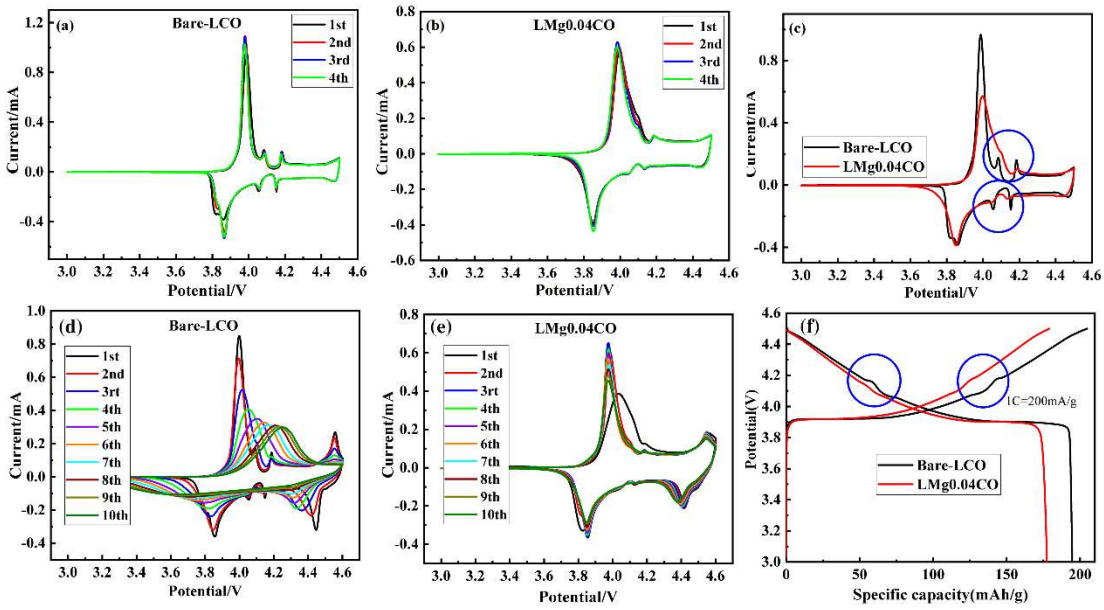

Figure 4 The CV curves of as-prepared electrode materials with the scan rate of 0.1mV/s from 3.0V to 4.5V: (a) Bare LCO, (b) LM0.04CO; The CV curves of as-prepared electrode materials with the scan rate of 0.1mV/s from 3.0V to 4.6V: (d) Bare LCO, (e) LM0.04CO; (c) and (f) the comparison of phase transition on first cycle CV curve corresponding with first cycle charging/discharging curve.

To reveal the oxidation reduction peaks of the cation and anion, typical cyclic voltammogram (CV) curves of the LCO and LM0.04CO cathode materials for lithium-ion batteries were tested in the voltage range from 3.0 to 4.5 V at a scan rate of 0.1 mVs^{-1}; the results are shown in Figure 4(a) and (b). When the cathode materials are charged at 4.5 V, neither material has a significant polarization phenomenon. However, when the cathode materials are charged at the highest voltage of 4.6 V, the bare LCO and LM0.04CO cathode materials show two different polarization trends, as shown in Figure 4(d) and (e). Clearly, compared with the bare LCO cathode material, the polarization phenomenon of the LM0.04CO cathode material greatly decreases, especially after 10 cycles, which also illustrates that the voltage decay is weakened.

Compared with bare LCO, the reversibility of the LM0.04CO sample redox peak between approximately 4.5 V and 4.6 V improves significantly due to the substitution of Mg^{2+} for Li, which illustrates the increase in oxygen stability. The CV curves almost overlap with the highly reproducible redox peaks, which illustrates the good reversibility of the LM0.04CO electrode material for lithium-ion batteries at high voltage, especially when charged to the highest voltage of 4.6 This result also verifies that the substitution of Mg^{2+} for Li can stabilize the layered structure and enhance the oxygen stability of high-voltage $LiCoO_2$. The energy barrier of Li^+ diffusion decreases due to the increase in the interlayer spacing, which is also conducive to stabilizing the layered structure and weakening the polarization phenomenon in the charge/discharge process.

In addition, compared with bare LCO, the transformation of the structure from the hexagonal phase to the monoclinic phase of the LM0.04CO cathode material is strongly inhibited: lithium ions shift from order to disorder, as shown in Figure 4(c) and (f), during the first cycle of the charge/discharge process. The CV curve of the first cycle is consistent with the first cycle of the charge/discharge curve marked with a blue circle. It is well known that the structure from the hexagonal phase to monoclinic phase has a great influence on the stability of the layered structure due to the order-disorder transition. This phenomenon is weakened, but the reversibility of the LM0.04CO electrode material for use in lithium-ion batteries is enhanced by doping Mg^{2+} at the Li^+ site, which is beneficial for improving the cycling performance of the electrode material.

2.3 First-principles calculations

First-principles calculations were performed by density functional theory (DFT) to understand the structural stability and migration energy barrier of the bare LCO and LM0.04CO electrode materials in the Li^+ extraction/insertion process. Figure S6(a) and (b) shows the DFT-optimized structure of the bare LCO and LM0.04CO materials. Based on this model, the projected density of states (DOS) analyses reveal that the breaking of symmetry leads to a significant change in the electronic band structure, as shown in Figure 5(56, 57). Compared with bare LCO, edge states appear near the Fermi level in the LM0.04CO cathode material. As a result, the band gap decreases from 2.1 to 1.3 eV. This decrease in the band gap can improve the electrical conductivity, which facilitates charge transfer for faster kinetics. Compared with the bare LCO, the upshift in the O p-band center of the LM0.04CO cathode material can strengthen the Co-O orbital hybridization, which benefits the stability of oxygen.(58).

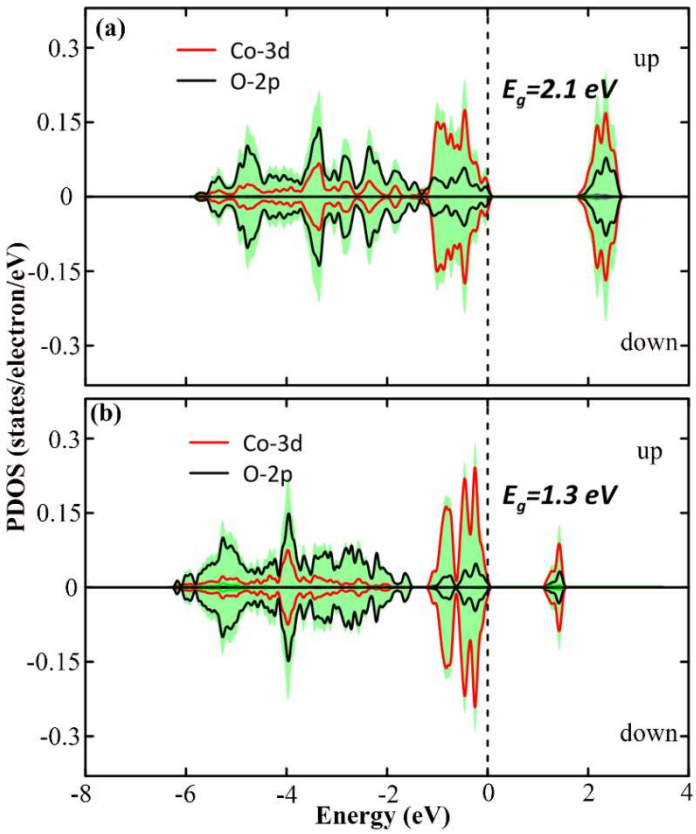

Figure 5 The calculated density of states (DOS) of bare LCO (a); LM0.04CO (b)

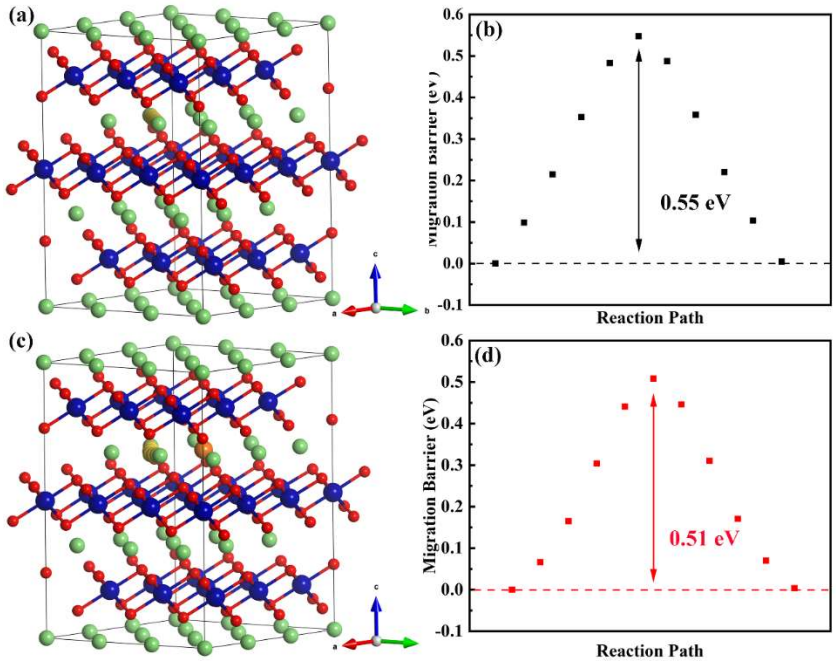

Figure 6 (a) Schematic diagrams of Li migration in bare LCO; (b) the migration barrier of Li migration in bare LCO; (c) Schematic diagrams of Li migration in LM0.04CO; (d) the migration barrier of Li migration in LM0.04CO

The migration of lithium ions is clearly revealed by DFT, and schematic diagrams of lithium-ion migration are shown in Figure 6. As shown in Figure 6(a) and (c), compared with the regular migration path of lithium ions in the bare LCO cathode material, the migration path of lithium ions is substantially changed in LM0.04CO by the substitution of Mg^{2+} for Li^{+}, which leads to the energy barrier of the migration decreasing from 0.55 eV to 0.51 eV, as shown in Figure 6(b) and (d). The decrease in the migration energy barrier means that the ratio of lithium-ion migration in the LM0.04CO sample becomes faster than that in the bare LCO sample, which illustrates the improvement in rate capacity(59).

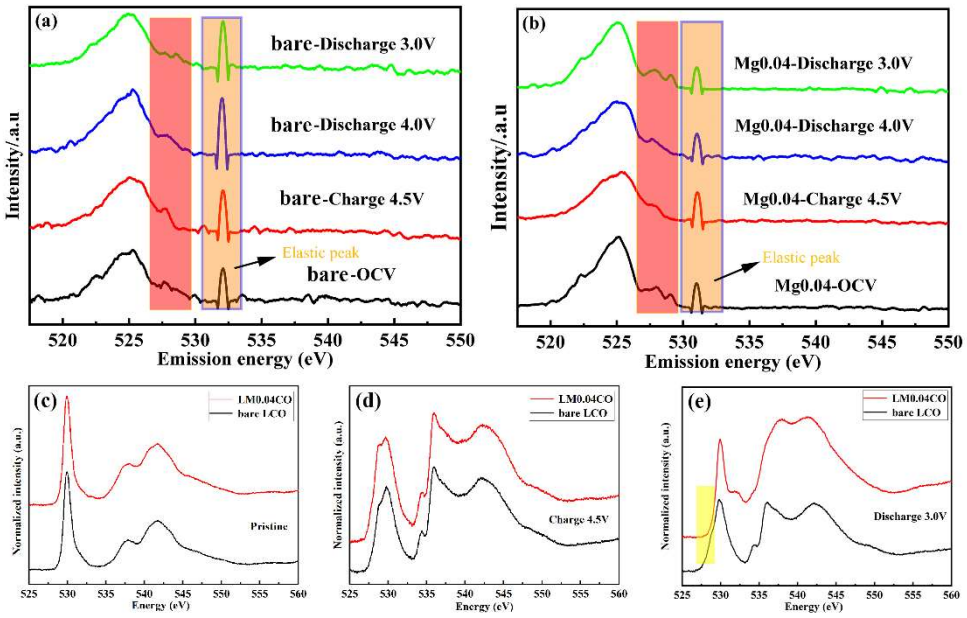

Figure 7 RIXS O K-edge spectra collected on bare LCO (a) and LM0.04CO (b) in Open Circuit Voltage (OCV)、Charge 4.5V、Discharge 4.0V、Discharge 3.0V；(c) the O k-edge of soft XAS of bare LCO and LM0.04CO at pristine state、(d) at the charge 4.5V state and (e) at the discharge 3.0V state in the TEY mode, respectively

To further verify the increased stability of oxygen by the substitution of Mg^{2+} for Li^{+}, RIXS O K-edge spectra measurements were performed for both electrode materials; these tests were recorded at an incident energy of 531 eV in the *ex situ* state of the OCV, along with a charge of 4.5 V, discharge of 4.0 V, and a discharge of 3.0 V, as shown in Figure 7(a) and (b). We clearly observe that there is no new peak at 523.5 eV when both materials are charged to 4.5 V and discharged to 2.0 V, which illustrates that oxygen may not or only slightly participates in the redox reaction. However, compared with the bare LCO material, the reduced intensity of the elastic peak implies the accumulation of a few oxygen holes in the LM0.04CO material during the charge/discharge process, which also reflects that the stability of oxygen from the side is enhanced by the substitution of Mg^{2+} for Li^{+}(26, 60, 61). In addition, as shown in Figure 7(c), (d) and

(e), soft XAS spectra were used to reveal the electronic structure of the oxygen atoms in the electrode materials in TEY mode, and Figure S7 shows the TFY mode. Compared with the bare LCO material, the change in the peak in the soft XAS spectra is not obvious with the pristine material and the material charged to a 4.5 V state in Figure 7(c) and (d). However, when discharged at 3.0 V, we can clearly observe that the pre-edge peak shape of bare LCO changes significantly compared with the LM0.04CO cathode material. The change in the pre-edge peak shape may indicate that the CoO_6 octahedron is distorted (irreversible structural transformation)(62). Therefore, the stability of the structural transformation and oxygen in the LM0.04CO electrode material is enhanced by the substitution of Mg^{2+} for Li^{+}, which benefits the extended cycling stability of the material.

To further investigate the reasons for the excellent electrochemical performance of the LM0.04CO material, electrochemical impedance spectroscopy (EIS) and the potentiostatic intermittent titration technique (PITT) were performed, as shown in Figure S8. EIS was tested at different frequencies ranging from 0 Hz to 100 kHz to obtain the Nyquist curves of both samples, as shown in Figure S8(a). The Rele value and the Rct value were fitted by the circuit, as clearly shown in the histogram in Figure S8(b). Rele represents the internal ohmic resistance and reveals the combined resistance of the liquid electrolyte, Li-metal anode, and Al-foil current collector. The semicircle at high frequencies along the Z' axis and the linear part at low frequencies represent the electrochemical reaction resistance (Rct) and diffusion-controlled Warburg impedance, respectively. Compared with the bare LCO cathode material, Rele and Rct are greatly

reduced in the LM0.04CO cathode material due to the substitution of Mg^{2+} for Li^{+}.

In addition, as shown in Figure S8(c) and (d), the two semicircles in the EIS spectra at high frequency and low frequency represent the movement of Li^{+} through the solid electrolyte interface (SEI) and the charge-transfer resistance in the electrode/electrolyte interface, respectively. Compared with the bare LCO sample, the charge-transfer resistance in the LM0.04CO cathode material clearly has little change with the increase in the number of cycles, which indicates the improvement in structural stability by the Mg "pillar". Moreover, the potentiostatic intermittent titration technique (PITT) was conducted to compare the Li^{+} diffusion coefficient, as shown in Figure S8(e) and (f). Compared with the bare LCO cathode material, we can see that the Li^{+} diffusion coefficient is also improved and Li ions have a stable diffusion coefficient at each voltage plateau by the substitution of Mg^{2+} for Li^{+}, corresponding to the improvement in the rate capability. This result is also consistent with the expansion of the interlayer spacing ($I_{(LiO2)}$) and the reduction in the lithium-ion migration energy barrier calculated by DFT.

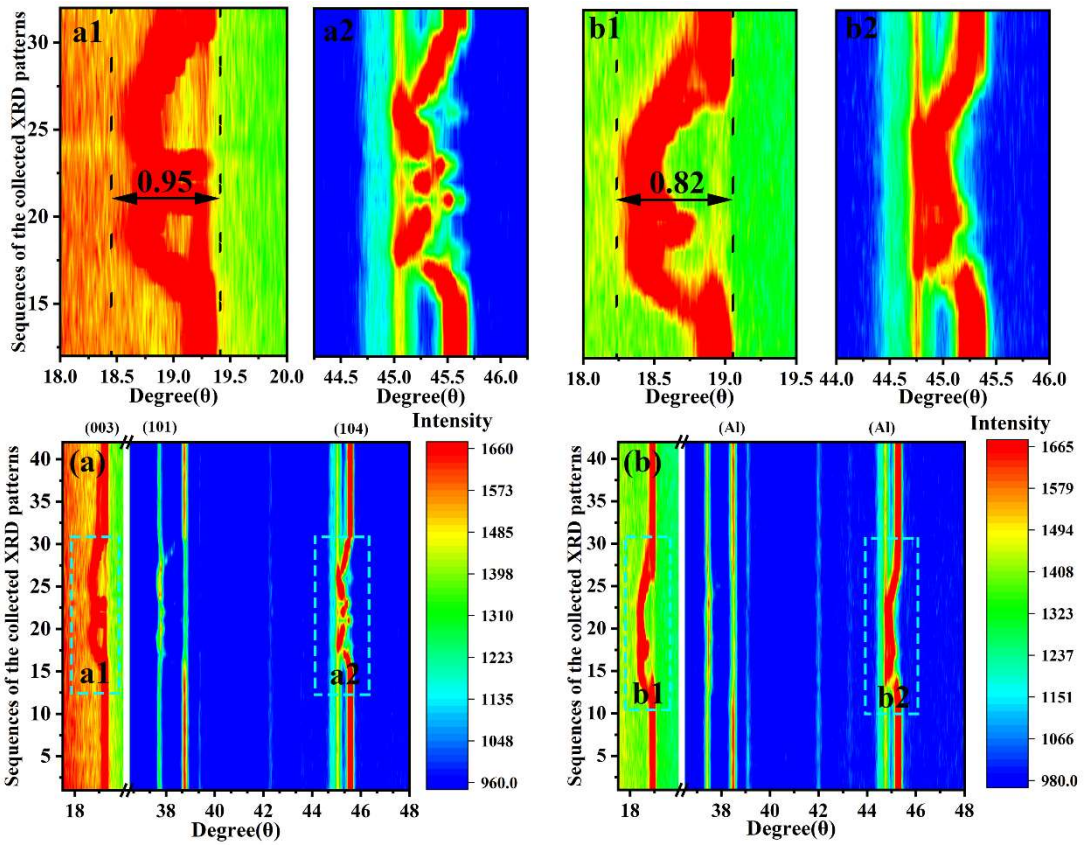

Figure 8 (a) *In situ* XRD patterns collected during the cyclic voltammograms of Bare LCO with the scan rate of 0.2 mV/s: a1(003) and a2(104) zooming in of frame selection area; (b) *In situ* XRD patterns collected during the cyclic voltammograms of LM0.04CO with the scan rate of 0.2 mV/s: b1(003) and b2(104) zooming in of frame selection area

To further reveal the stability of the layered structure, especially at high voltages, the electrode material is charged to 4.5 V. The layered structure evolution of the electrode materials was investigated by *in situ* XRD patterns during the Li-ion intercalation/extraction process with the following parameters: a step width of 0.01°, a voltage range of 3.0 V to 4.5 V, and a cyclic voltammogram curve scan rate of 0.2 mV/s. The sequences of the collected *in situ* XRD patterns from "1" to "40" are shown in Figure S9. In the XRD pattern of the hexagonal-layered structure of the $LiCoO_2$ material, the shifting in the (003) peak represents the change in the *c* value, while (101)

represents the change in the *a* and *b* values(27, 63, 64). Amatucci et al. reported that the value of the lattice parameter *c* clearly changed during the charge/discharge process (65). Hence, the main peaks were analyzed in the range from 18° to 48°, as shown in Figure 8(a) and (b). In contrast, the (003) peak of bare LCO shows a greater variation range (0.95) than that of the LM0.04CO (0.82) cathode material, as shown in the magnified areas a1 and b1. When charging to approximately 4.5 V, the (104) peak in the bare LCO material becomes discontinuous and disorganized, so the change is larger than that in the LM0.04CO material, as shown in the magnified areas a2 and b2. The different evolution of the (003) peak and (104) peak in both samples during charging to approximately 4.5 V indicates that the volume change of bare LCO is larger than that of LM0.04CO during the charge/discharge process, which leads to severe structural degradation (such as an irreversible phase transition), especially after long-term cycling(66). This result might benefit from the Mg "pillar" in the interlayer spacing ($I_{(LiO2)}$), which not only provides a fast lithium-ion channel but also enhances the stability of the layered structure. The stability of oxygen in the host structure is also important, especially in maintaining the hexagonal-layered structure of the $LiCoO_2$ material at high voltage.

To verify the conclusion obtained by the *in situ* XRD patterns, *ex situ* XRD patterns of the bare LCO, LM0.04CO and LCM0.04O cathode materials were further tested, as shown in Figure S10(a), (c) and (e), respectively. Compared with the pristine electrode materials, the original O3-type phase structure of the cathode materials was maintained at any potential. The refinement results of the XRD patterns when the materials are

charged to 4.5 V are shown in Figure S10(b), (d) and (f). Although the *ex situ* XRD patterns of the first cycle cannot explain the reversibility of the electrode materials, the change in the interlayer spacing ($I_{(LiO2)}$) of the microcrystal structure is obvious when charged at 4.5 V. Especially in the bare LCO cathode material, the interlayer spacing ($I_{(LiO2)}$) is largely reduced to 0.9818 Å after charging to 4.5 V, but the interlayer spacing ($I_{(LiO2)}$) in the LM0.04CO electrode material changes very little owing to the Mg "pillar", as shown in Figure S11. The continuous intercalation/extraction of lithium ions from the interlayer spacing of the crystal structure will lead to structural damage (especially the decrease in the interlayer spacing); however, owing to the existence of the Mg^{2+} "pillar", the interlayer spacing ($I_{(LiO2)}$) can maintain the integrity of the crystal structure in the LM0.04CO cathode material; in particular, the structural stability is maintained even after long cycles.

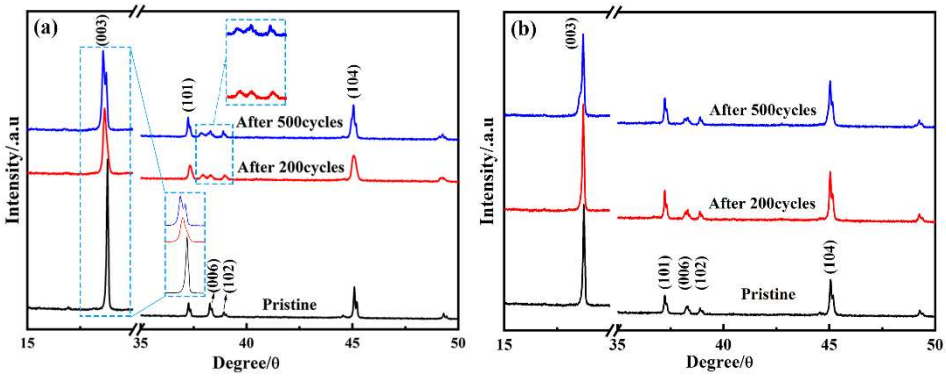

Figure 9 The comparison of XRD patterns collected before and after cycles at 5C: (a) bare LCO, the insert shows the change of the (003) peak; (b) LM0.04CO samples

Compared with the bare LCO sample (impurity peak appears near the (003) peak after 500 cycles), the XRD pattern of LM0.04CO maintains the original peak shape before and after cycling, as shown in Figure 9, which is also the reason for its higher

capacity retention ratio. Moreover, for bare LCO in Figure 9(a), the (006) and (102) peaks (characteristic peaks of a hexagonal-layered structure) undergo obvious changes, which indicate the destruction of the layered structure after 200 cycles, while the peaks in the LM0.04CO electrode still evidently exist in Figure 9(b). As shown in Figure S12, the cracks, breakage, dissolution and fracture caused by the stress and strain of Li^+ migration (the cyclic expansion and contraction of the interlayer spacing ($I_{(LiO2)}$)) all appear in the bare LCO sample but not in LM0.04CO through the comparison of SEM images after 200 and 500 cycles at 5C; these conditions are unfavorable to cycling performance and result in the irreversible loss of capacity, which agrees with that in Figure 2(d). Therefore, the Mg^{2+} "pillar" not only does not affect the migration of lithium ions but also enhances the stability of the structure and reduces the stress and strain of the crystal structure caused by the diffusion of lithium ions. The above behavior is conducive to maintaining the layered structure and improving the cycling performance of the cathode materials.

3 Conclusion

In summary, the different effects of Mg substitution at Li and Co sites in high-voltage $LiCoO_2$ have been systematically investigated. Mg doping can improve the electrochemical performance, but the substitution of Mg for Li or Co has a different impact on the enhancement. The substitution of Mg for Li displays superior stability during long-term cycling: 85.6% capacity retention after 500 cycles at 5C between 3.0 V and 4.5 V. The substitution of Mg for Li can provide a "pillar" to stabilize the crystal structure and reduce the energy barrier of Li^+ diffusion due to the increase in the

interlayer spacing. Moreover, the decrease in $S_{(MO2)}$ that is induced by the substitution of Mg for Li also enhances the stability of the layered structure. The stress and strain of the crystal structure caused by the diffusion of lithium ions is further decreased during long-term cycling, and the destruction of the CoO_6 octahedron is significantly inhibited. This study provides new insight into improving the electrochemical performance by designing and optimizing the occupation of dopants.

Acknowledgements

This work was supported by National Natural Science Foundation of China (Grant No. 11975238, 22005302 and 11575192), the Scientific Instrument Developing Project (Grant No.ZDKYYQ20170001), the International Partnership Program (Grant No. 211211KYSB20170060 and 211211KYSB20180020) of the Chinese Academy of Sciences, and Natural Science Foundation of Beijing Municipality (Grant No. 2182082). This work was also supported by the Fundamental Research Funds for the Central Universities and the China Postdoctoral Science Foundation (2020M680648).

Conflict of interest The authors declare that they have no conflict of interest.

Reference

1. F. Wu, J. Maier and Y. Yu, *Chem. Soc. Rev.*, **49**, 1569 (2020).
2. H. Ji, J. Wu, Z. Cai, J. Liu, D.-H. Kwon, H. Kim, A. Urban, J. K. Papp, E. Foley, Y. Tian, M. Balasubramanian, H. Kim, R. J. Clément, B. D. McCloskey, W. Yang and G. Ceder, *Nat. Energy*, **5**, 213 (2020).
3. J. Hou, M. Yang, D. Wang and J. Zhang, *Adv. Energy Mater.*, **10**, 1904152 (2020).
4. A. Mauger, C. M. Julien, M. Armand and K. Zaghib, *Adv. Energy Mater.*, 2000773 (2020).
5. F. Jiao, K. M. Shaju and P. G. Bruce, *Angew. Chem.*, **117**, 6708 (2005).
6. M. Zhang, M. Tan, H. Zhao, S. Liu, X. Shu, Y. Hu, J. Liu, Q. Ran, H. Li and X. Liu, *Appl. Surf. Sci.*, **458**, 111 (2018).
7. H. Zhao, J. Wang, G. Wang, S. Liu, M. Tan, X. Liu and S. Komarneni, Ceramics International, 43, 10585 (2017).
8. H. Zhao, S. Liu, X. Liu, M. Tan, Z. Wang, Y. Cai and S. Komarneni, *Ceram. Int.*, **42**, 9319 (2016).
9. H. Zhao, Y. Nie, Y. Li, T. Wu, E. Zhao, J. Song and S. Komarneni, *Ceram. Int.*, **45**, 17183 (2019).

10. H. Zhao, X. Gao, Y. Li, Q. Ran, C. Fu, Y. Feng, J. Liu, X. Liu and J. Su, *Ceram. Int*., **45**, 17591 (2019).
11. H. Zhao, S. Liu, Z. Wang, Y. Cai, M. Tan and X. Liu, *Ceram. Int*., **42**, 13442 (2016).
12. H. Zhao, S. Liu, Y. Cai, Z. Wang, M. Tan and X. Liu, *J. Alloys and Compounds*, **671**, 304 (2016).
13. S. Saha, G. Assat, M. T. Sougrati, D. Foix, H. Li, J. Vergnet, S. Turi, Y. Ha, W. Yang, J. Cabana, G. Rousse, A. M. Abakumov and J.-M. Tarascon, *Nat. Energy*, **4**, 977 (2019).
14. W. Li, S. Lee and A. Manthiram, *Adv. Mater*., e2002718 (2020).
15. Q. Ran, H. Zhao, Y. Hu, S. Hao, Q. Shen, J. Liu, H. Li, Y. Xiao, L. Li, L. Wang and X. Liu, *ACS appl. Mater. Inter*., **12**, 9268 (2020).
16. Q. Ran, H. Zhao, Y. Hu, S. Hao, J. Liu, H. Li and X. Liu, *J. Alloys and Compounds*, **834**, 155099 (2020).
17. Q. Ran, H. Zhao, Q. Wang, X. Shu, Y. Hu, S. Hao, M. Wang, J. Liu, M. Zhang, H. Li, N. Liu and X. Liu, *Electrochim. Acta*, **299**, 971 (2019).
18. Q. Ran, H. Zhao, X. Shu, Y. Hu, S. Hao, Q. Shen, W. Liu, J. Liu, M. Zhang, H. Li and X. Liu, *ACS Appl. Energy Mater*., **2**, 3120 (2019).
19. Y. Ding, Z. P. Cano, A. Yu, J. Lu and Z. Chen, *Electrochem. Energy Rev*., **2**, 1 (2019).
20. Y. Lyu, X. Wu, K. Wang, Z. Feng, T. Cheng, Y. Liu, M. Wang, R. Chen, L. Xu, J. Zhou, Y. Lu and B. Guo, *Adv. Energy Mater*., 2000982 (2020).
21. K. Wang, J. Wan, Y. Xiang, J. Zhu, Q. Leng, M. Wang, L. Xu and Y. Yang, *J. Power Sources*, **460**, 228062 (2020).
22. F. Wang, Y. Lin, L. Suo, X. Fan, T. Gao, C. Yang, F. Han, Y. Qi, K. Xu and C. Wang, *Energy. Environ. Sci*., **9**, 3666 (2016).
23. R. Gu, T. Cheng, Z. Ma, R. Qian, Y. Lyu, A. Nie and B. Guo, *J. Alloys and Compounds*, **803**, 348 (2019).
24. J. Lim, A. Choi, H. Kim, S. W. Doo, Y. Park and K. T. Lee, *J. Power Sources*, **426**, 162 (2019).
25. A. Zhou, W. Wang, Q. Liu, Y. Wang, X. Yao, F. Qing, E. Li, T. Yang, L. Zhang and J. Li, *J. Power Sources*, **362**, 131 (2017).
26. J.-N. Zhang, Q. Li, C. Ouyang, X. Yu, M. Ge, X. Huang, E. Hu, C. Ma, S. Li, R. Xiao, W. Yang, Y. Chu, Y. Liu, H. Yu, X.-Q. Yang, X. Huang, L. Chen and H. Li, *Nat. Energy*, **4**, 594 (2019).
27. L. Wang, J. Ma, C. Wang, X. Yu, R. Liu, F. Jiang, X. Sun, A. Du, X. Zhou and G. Cui, *Adv. Sci*., **6**, 1900355 (2019).
28. Y. Wang, Q. Zhang, Z. C. Xue, L. Yang, J. Wang, F. Meng, Q. Li, H. Pan, J. N. Zhang, Z. Jiang, W. Yang, X. Yu, L. Gu and H. Li, *Adv. Energy Mater*., 2001413 (2020).
29. S. Sharifi‐Asl, F. A. Soto, T. Foroozan, M. Asadi, Y. Yuan, R. Deivanayagam, R. Rojaee, B. Song, X. Bi, K. Amine, J. Lu, A. Salehi‐khojin, P. B. Balbuena and R. Shahbazian‐Yassar, *Adv. Funct. Mater*., **29**, 1901110 (2019).
30. J. Qian, L. Liu, J. Yang, S. Li, X. Wang, H. L. Zhuang and Y. Lu, *Nat. Commun*., **9**, 4918 (2018).
31. Y. Lee, A. J. Woo, K.-S. Han, K. S. Ryu, D. Sohn, D. Kim and H. Lee, *Electrochim. Acta*, **50**, 491 (2004).
32. K. Sivajee Ganesh, B. Purusottam reddy, P. Jeevan Kumar and O. M. Hussain, *J. Electroanalytical Chem*., **828**, 71 (2018).
33. M. C. Rao and O. M. Hussain, *J. Alloys and Compounds*, **491**, 503 (2010).
34. S. Valanarasu and R. Chandramohan, *J. Alloys and Compounds*, **494**, 434 (2010).
35. P. Ghosh, S. Mahanty and R. N. Basu, *Electrochim. Acta*, **54**, 1654 (2009).
36. A. Zhou, Y. Lu, Q. Wang, J. Xu, W. Wang, X. Dai and J. Li, *J. Power Sources*, **346**, 24 (2017).
37. A. Zhou, Q. Liu, Y. Wang, W. Wang, X. Yao, W. Hu, L. Zhang, X. Yu, J. Li and H. Li, *J. Mater. Chem. A*, **5**, 24361 (2017).
38. N. Taguchi, T. Akita, K. Tatsumi and H. Sakaebe, *J. Power Sources*, **328**, 161 (2016).

39. J. Zhang, R. Gao, L. Sun, H. Zhang, Z. Hu and X. Liu, *Electrochim. Acta*, **209**, 102 (2016).
40. X. Pu and C. Yu, *Nanoscale*, **4**, 6743 (2012).
41. R. Zhao, J. Zhang, G.-H. Lee, K. Zhang, V. W.-h. Lau, J.-J. Lee, I. Moudrakovski, Y.-L. Yang, F. Zou, M. Park, I. M. Hung and Y.-M. Kang, *J. Mater. Chem. A*, **8**, 12424(2020).
42. J. Kim, H. Kang, N. Go, S. Jeong, T. Yim, Y. N. Jo, K. T. Lee and J. Mun, *J. Mater. Chem. A*, **5**, 24892 (2017).
43. Y.-S. Hong, X. Huang, C. Wei, J. Wang, J.-N. Zhang, H. Yan, Y. S. Chu, P. Pianetta, R. Xiao, X. Yu, Y. Liu and H. Li, *Chem*, **6**, 1(2020).
44. Y. Huang, Y. Zhu, H. Fu, M. Ou, C. Hu, S. Yu, Z. Hu, C. T. Chen, G. Jiang, H. Gu, H. Lin, W. Luo and Y. Huang, *Angew. Chem.* (2020), DOI: 10.1002/anie.202014226.
45. H. J. Kim, Y. Park, Y. Kwon, J. Shin, Y.-H. Kim, H.-S. Ahn, R. Yazami and J. W. Choi, *Energy. Environ. Sci*., **13**, 286 (2020).
46. J. Rodriguez-Carjaval, *An Introduction to the Program FULLPROF2000*, Version, France (2001).
47. Q. Li, D. Ning, D. Zhou, K. An, D. Wong, L. Zhang, Z. Chen, G. Schuck, C. Schulz, Z. Xu, G. Schumacher and X. Liu, *J. Mater. Chem. A*, **8**, 7733(2020).
48. Z.-Y. Li, R. Gao, J. Zhang, X. Zhang, Z. Hu and X. Liu, *J. Mater. Chem. A*, **4**, 3453 (2016).
49. W. Kong, H. Wang, Y. Zhai, L. Sun and X. Liu, *J. Phy. Chem. C*, **122**, 25909 (2018).
50. H. Li, X. Yu, Y. Bai, F. Wu, C. Wu, L.-Y. Liu and X.-Q. Yang, *J. Mater. Chem. A*, **3**, 9578 (2015).
51. H. Li, Y. Bai, F. Wu, Q. Ni and C. Wu, *ACS appl. Mater. Inter*., **8**, 27779 (2016).
52. H. Li, H. Tang, C. Ma, Y. Bai, J. Alvarado, B. Radhakrishnan, S. P. Ong, F. Wua, Y. S. Meng and C. Wu, *Chem. Mater*., **30**, 2498 (2018).
53. X. Liu, Y. Tan, W. Wang, C. Li, Z. W. Seh, L. Wang and Y. Sun, *Nano Lett*., **20**, 4558 (2020).
54. K. Nie, X. Sun, J. Wang, Y. Wang, W. Qi, D. Xiao, J.-N. Zhang, R. Xiao, X. Yu, H. Li, X. Huang and L. Chen, *J. Power Sources*, **470**, 228423 (2020).
55. W. Kong, H. Wang, L. Sun, C. Su and X. Liu, *Appl. Surf. Sci*., **497**, 143814 (2019).
56. Z. Zhang, C. Liu, C. Feng, P. Gao, Y. Liu, F. Ren, Y. Zhu, C. Cao, W. Yan, R. Si, S. Zhou and J. Zeng, *Nano Lett*., **19**, 8774 (2019).
57. X. Wang, X. Fan, X. Yu, S. Bak, Z. Shadike, I. Waluyo, A. Hunt, S. D. Senanayake, H. Li, L. Chen, C. Wang, R. Xiao, E. Hu and X. Q. Yang, *Adv. Funct. Mater*., 2001633 (2020).
58. M. Yoon, Y. Dong, Y. Yoo, S. Myeong, J. Hwang, J. Kim, S. H. Choi, J. Sung, S. J. Kang, J. Li and J. Cho, Adv. Funct. Mater., **30**, 1907903 (2019).
59. Q. Ni, L. Zheng, Y. Bai, T. Liu, H. Ren, H. Xu, C. Wu and J. Lu, ACS Energy Lett., **5**, 1763 (2020).
60. K. Luo, M. R. Roberts, N. Guerrini, N. Tapia-Ruiz, R. Hao, F. Massel, D. M. Pickup, S. Ramos, Y. S. Liu, J. Guo, A. V. Chadwick, L. C. Duda and P. G. Bruce, *J. Am. Chem. Soc*., **138**, 11211 (2016).
61. L. C. Duda and K. Edström, *J. Electron Spectroscopy and Related Phenomena*, **221**, 79 (2017).
62. Q. Li, D. Zhou, L. Zhang, D. Ning, Z. Chen, Z. Xu, R. Gao, X. Liu, D. Xie, G. Schumacher and X. Liu, *Adv. Funct. Mater*., **29**, 1806706 (2019).
63. Q. Liu, X. Su, D. Lei, Y. Qin, J. Wen, F. Guo, Y. A. Wu, Y. Rong, R. Kou, X. Xiao, F. Aguesse, J. Bareño, Y. Ren, W. Lu and Y. Li, *Nat. Energy*, **3**, 936 (2018).
64. T. Cheng, Z. Ma, R. Qian, Y. Wang, Q. Cheng, Y. Lyu, A. Nie and B. Guo, *Adv. Funct. Mater*., 2001974 (2020).
65. G. G. Amatucci, J. M. Tarascon, L. C. Klein, *J. Electrochem. Soc*. **143**,1114(1996).
66. S. Li, K. Li, J. Zheng, Q. Zhang, B. Wei and X. Lu, *J. Phy. Chem. Lett*., **10**, 7537 (2019).